A novel explanation of increased conductivity in annealed Al-doped ZnO: an insight into migration of aluminum and displacement of zinc

Authors:

A. Momot[a], M.N. Amini[c], G. Reekmans[b], P. Adriaensens[b], D. Lamoen[c], B. Partoens[c], D. R. Slocombe[d], K. Elen[a], A. Hardy[a], M. K. Van Bael[a]

Affiliations

a) UHasselt - Hasselt University, Institute for Materials Research (IMO-IMOMEC), Inorganic and Physical Chemistry, Agoralaan, 3590 Diepenbeek, Belgium

b) UHasselt - Hasselt University, Institute for Materials Research (IMO-IMOMEC), Applied and Analytical Chemistry, Agoralaan, 3590 Diepenbeek, Belgium

c) CMT & EMAT, Department of Physics, University of Antwerp, Groenenborgerlaan 171, B-2020 Antwerp, Belgium

d) School of Engineering, Cardiff University, Queen's Buildings, The Parade, Cardiff, CF24 3AA, UK.

Abstract:

A combined experimental and first-principles study is performed to study the origin of the conductivity in ZnO:Al nanoparticles synthesized under controlled conditions by a reflux route using benzylamine as a solvent. The experimental characterization of the samples by Raman, nuclear magnetic resonance (NMR) and conductivity measurements indicate that upon annealing in nitrogen, the Al at interstitial positions migrates to the substitutional positions, creating at the same time Zn interstitials. We give evidence for the fact that the formed complex of Al_{Zn} and Zn_i is the origin of the Knight shifted peak (KS) we observe in ^{27}Al NMR. As far as we know, the role of this complex has not been discussed in literature until now. However, our first-principles calculations show that such a complex is indeed energetically favoured over the isolated Al interstitial positions. In our calculations we also address the charge state of the Al interstitials. Further, the Zn interstitials can migrate from the Al_{Zn} and possibly also form Zn clusters, leading to the observed increased conductivity.

INTRODUCTION

Aluminum doped zinc oxide (AZO or ZnO:Al) is a transparent conductive oxide (TCO) that in recent years [1-3] has attracted attention as a potential replacement for indium tin oxide (ITO), given its low resistivity (~10^{-4}Ωcm) and high transparency up to 90% [4]. Moreover, ZnO is a favorable material due to its low toxicity and high abundance. Also, it can be used in the form of thin films or nanoparticles in various fields, such as antistatic coatings, electrodes for photovoltaics, or gas sensors [5-8]. In order to achieve this, AZO films and particles have been synthesized by various methods, optimally providing the desired low resistivity, high transparency, flexibility and tunable infrared absorption [9-15].

Often, an effect of processing conditions on the ZnO conductivity has been observed [16-23]. In many cases, annealing in vacuum, hydrogen or inert conditions is applied to enhance the conductivity. However, the mechanisms behind the increased conductivity in the different processing conditions are not yet fully understood. For example, C. Guillen and J. Herrero [12] report that they achieve an increased conductivity of a magnetron sputtered material after annealing in vacuum. They establish a relation between the carrier concentration and mobility, but not the reason for the increased carrier concentration. Similarly, Hartner et al. [13] have shown a way of successfully synthesizing aluminum-doped zinc oxide nanoparticles by means of chemical vapor deposition, and have shown that incorporation of Al into the crystalline lattice is possible up to 7% upon synthesis. However, they do not give an explanation why the conductivity increases subsequently to annealing.

On the other hand, many theoretical studies provide ideas of how different defects can affect the conductivity in ZnO. Many defects are found to affect the conductivity, for instance the influence of aluminum itself, but also hydrogen impurities, oxygen vacancies, and Zn interstitials have been reported [1, 11, 24-26]. Although native point defects are unavoidable in ZnO, it is often assumed that they have only a minor effect on the conductivity of ZnO. An overview of native point defects in zinc oxide and their contribution to the n-type conductivity in zinc oxide is reviewed in [25]. Oxygen vacancies, although often used as an explanation to the inherent n-type conductivity in zinc oxide, are deep donors and have high formation energies in n-type ZnO [27]. They are believed to be mostly present in p-type ZnO as compensating defects. Oxygen interstitials are deep acceptors, with high formation energies and thus also cannot be responsible for n-type conductivity in zinc oxide. Another widely discussed defect is interstitial zinc. Although potentially able to be the cause of n-type conductivity since it is a shallow donor, interstitial Zn has a high formation energy,

and is claimed to be thermally unstable as an isolated point defect [25]. Zinc vacancies on the other hand are acceptors and only decrease the conductivity in n-type ZnO.

In contrast to these defects, it has been shown that hydrogen impurities can be the cause of n-type conductivity in zinc oxide, since a hydrogen impurity has a low formation energy in zinc oxide and acts exclusively as a donor. Moreover, it can form a complex with an oxygen vacancy, which will also act as a shallow donor [26].

Besides, it has been reported that Zn interstitial clusters can also be responsible for n-type conductivity in zinc oxide, as shown by Gluba et al. [24]. The proposed theory suggests that zinc atoms occupy neighboring interstitial spaces in the ZnO crystalline lattice and form clusters of 5-8 atoms. Such a cluster is then stable, as opposed to single Zn atom defects.

By using extrinsic dopants, such as aluminum, the n-type conductivity can be increased even further. Aluminum can occupy three different positions in the wurzite structure of zinc oxide: the substitutional position Al_{Zn}, the tetrahedral interstitial position Al_{Td} and the octahedral interstitial position Al_{Oh}. To this day, the charge of the Al interstitial defects is debated between being 1+ or 3+. It is only widely recognized that substitutional Al is effective as a stable n-type shallow donor in a 1+ charge state. [28, 29] On the other hand, the contribution of interstitial Al dopants to the conductivity in AZO is still highly questioned. For example, Kemmitt et al. [30] suggest that the Al ions behave as an acceptor in both octahedral and tetrahedral interstitial positions, and decrease conductivity, which is contradicted by theoretical predictions, claiming that Al in the octahedral and tetrahedral interstitial positions is in a 3+ charge state, and thus should increase the charge carrier concentration [31].

Many studies have been carried out to characterize AZO samples, applying, among others, techniques such as NMR, Raman spectroscopy and Rutherford backscattering [32-36]. They have confirmed that incorporation of aluminum into the crystalline lattice can occur at different sites, as mentioned above. Oga and Kaida [33, 37] have shown that, in implantation experiments, also the displacement of zinc from its position in the crystalline lattice is possible, and that it can have a strong effect on the conductivity.

Characterization by the NMR technique is in particular useful to study the oxygen coordination around the Al atoms in the sample, and allows to determine the relative concentration between the three possible Al positions in the ZnO lattice. Apart from the peaks indicating this coordination, some studies [28, 38] have also reported the observation of a Knight shifted (KS) signal in their NMR results. While the mechanism of appearance of this signal in metals has been explained [39, 40], the exact origin of this signal in zinc oxide samples is not yet understood.

Previous works show that different synthesis conditions yield a different Al distribution in the crystalline lattice, which in turn leads to different conductivities [41, 42]. H. Damm et al. have shown that the formation of conductive layers of aluminum-doped zinc oxide is a complicated process involving many factors. For instance it has been shown that reductive annealing not only induces morphological changes, but also contributes to redistribution of aluminum in the crystalline lattice and a change of the oxygen stoichiometry in the layers [43].

Finally, Russo et al. [44] have shown that the incorporation of Al into zinc oxide under different oxygen pressures yields significantly different results in terms of Raman spectra, which can be related to the electronic properties of ZnO. They particularly notice that while the zinc sub-lattice is less sensitive to oxygen pressure and reaches order at low oxygen pressures,

the oxygen sub-lattice gives significantly different results in terms of order with varying oxygen pressures. Also they noticed that the presence of aluminum favors the formation of oxygen vacancies.

All these findings suggest that the doping mechanism for aluminum-doped zinc oxide is hard to study in experimental conditions, since various properties of zinc oxide change with addition of the dopant and change of synthesis conditions. This is further emphasized by the difficulty of characterizing local defects in the crystalline lattice. To gain a better understanding of the origin of the conductivity in AZO, we report in this manuscript a combined theoretical and experimental study in which ZnO:Al nanoparticles, synthesized under controlled conditions by a reflux route using benzylamine as a solvent, are used as a model system. The experimental characterization of the samples by Raman, NMR and conductivity measurements indicate that upon annealing, the Al at interstitial positions migrate to the substitutional positions, creating at the same time Zn interstitials. We give evidence for the fact that the formed complex of Al_{Zn} and Zn_i is the origin of the observed KS peak in the NMR spectrum. Al_{Zn} as well as Zn_i are both shallow donors, therefore their complex might have a very high formation energy. However, our calculations show that such a complex is energetically favoured over the isolated Al interstitial. The Zn interstitials can also form Zn clusters, leading to the observed increased conductivity. In our calculations we also address the charge state of the Al interstitials.

Experimental details

SYNTHESIS

AZO nanoparticles were synthesized using a method previously described by Kelchtermans et al. [42]. In order to obtain 0.5 mol% aluminum doped zinc oxide nanospheres by a solvolysis

reaction in a reflux setup, 1g of $Zn(acac)_2$ hydrate was mixed with 0.0057g of Al(acac) hydrate in 40 ml of benzyl amine and heated to boiling point (nominal temperature 185°C). After reaching the boiling point the mixture was refluxed for 4 hours while stirring. After cooling down to room temperature, the mixture was centrifuged to precipitate the particles, and the particles were then washed three times with ethanol and twice with water. After washing, the obtained powder was dried in an oven at 60°C. The dried powder was divided into two parts allowing the same starting material to be used in subsequent experiments and analysis. One part of the powder was analyzed as-synthesized, and the rest underwent the following thermal treatment. This second part of the powder was annealed in dynamic nitrogen atmosphere (100 ml/min) for 10 minutes at 400°C in a tube furnace. During the annealing procedure the temperature ramp was 10°C per minute, and after the annealing time was over, the furnace was left to cool down naturally.

CHARACTERIZATION

The Al/Zn ratio in the powders was determined by inductively-coupled plasma atomic emission spectrometry (ICP-AES) using a Perkin Elmer Optima 8300 DV. The sample preparation was performed by making a stock solution of with a concentration of 1g/L of AZO in 5% nitric acid, and subsequently diluting it so that the concentration of Zn or Al would be in the range of 1 to 10 ppm. Calibration was made using stock solutions of Zn and Al.

X-Ray diffraction (XRD) was carried out in a Siemens D5000 X-Ray powder diffractometer.

Particle size and shape analysis was carried out using transmission electron microscopy (TEM), carried out on FEI Tecnai Spirit at an acceleration voltage of 120 kV. The sample was

prepared by dispersing a small amount of nanopowder in ethanol, and deposited on a carbon-film coated copper mesh and dried.

Using Fourier-transform infrared spectroscopy (FT-IR Bruker Vertex 70 FT-IR spectrometer) the presence of charge carriers was analyzed. The transmittance of the KBr pellets containing 0,5% AZO was measured in the interval of 4000 – 400 cm^{-1}.

Aluminum-27 solid-state MAS NMR spectra were acquired on an Agilent VNMRS DirectDrive 400MHz spectrometer (9.4 T wide bore magnet) equipped with a T3HX 3.2mm probe dedicated for small sample volumes and high decoupling powers. Magic angle spinning (MAS) was performed at 18 kHz in ceramic rotors of 3.2mm (22 µl). $AlCl_3$ was used to calibrate the aluminum chemical shift scale (0 ppm). The T_{1Al} relaxation decay times were measured by using the inverse recovery method.

A resonant microwave cavity perturbation technique (MCPT) was used to determine the microwave conductivity of the samples. To this end, a quartz tube filled with the sample was inserted into an aluminum TM_{010} mode resonant cavity. The measurements were carried out as described in [45].

Raman spectra were obtained using a Horiba Jobin Yvon T64000 Raman spectrometer in subtractive mode, equipped with a BXFM Olympus 9/128 microscope and a Horiba JY Symphony CCD detector and a 488 nm Lexell SHG laser.

Computational details

FIRST-PRINCIPLES CALCULATIONS

The calculations are performed using first-principles density functional theory (DFT) using the Perdew–Burke–Ernzerhof functional (PBE) [46] and the screened hybrid functional of Heyd, Scuseria, and Ernzerhof (HSE06) [47], as implemented in the Vienna ab initio simulation package [48, 49]. The hybrid functional has shown to yield rather accurate band gaps and reliable defect formation energies in semiconductors [50, 51]. This is important, since the introduction of defects can involve the occupation of levels in the band gap and a correct value of the formation energy depends sensitively on the position of these defect levels and thus on the value of the band gap. Thus the structural optimizations, band gap calculation, and formation energy calculations throughout the work are performed with the HSE06 functional. Electron-ion interactions are treated using projector augmented wave potentials [52-54]. A large supercell of wurtzite ZnO consisting of 108 atoms is used (3×3×3 unit cells). The Zn ($4s^2 3d^{10}$), O ($2s^2 2p^6$), and Al ($3s^2 3p^1$) electrons are treated as valence electrons. We have used an optimized 37.5% mixing of Hartree-Fock exchange mixing in the HSE06 functional to obtain the experimental band gap [55]. Proper convergence of the formation energy is reached when the energy cutoff for the plane wave basis is set to 400 eV, and a k-mesh of 2×2×2 based on the Monkhorst-Pack scheme[56] is used to sample the Brillouin zone of the supercell. The convergence of the self-consistent iterations is assumed when the total energy difference between cycles is less than 10^{-4} eV, and all atoms in the supercell are allowed to relax until the residual forces per atom are less than 0.05 eV $Å^{-1}$, which is sufficient for the purposes of the present work. The charge correction scheme proposed in [57] and utilized in [58] has been applied to correct for the spurious interaction between a charged defect and its periodic images.

DEFECT FORMATION ENERGIES

The formation energy of a point defect or impurity plays an essential role in the determination of its thermodynamic stability and its equilibrium concentration. The formation energy of a defect or impurity D in charge state q is calculated as the difference between the total energy of the stable pure supercell $E_{tot}[bulk]$ and the relaxed defect supercell $E_{tot}[D^q]$ at constant volume, and is defined in a standard way [59, 60],

$$E_f[D^q] = E_{tot}[D^q] - E_{tot}[bulk] + \sum_i n_i\mu_i + q[E_F + E_V + \Delta V] + \Delta E_{el}^q. \qquad (1)$$

Where n_i specifies the number of atoms of type i that have been added ($n_i < 0$) or removed ($n_i > 0$) from the supercell, and μ_i are the chemical potentials of matching species. E_F is the Fermi level with respect to the top of the valence band, E_V . ΔV aligns the potentials in the perfect and doped supercells in a region far from the defect [61, 62], and ΔE_{el}^q is the charge correction term for the energy.

Equation (1) indicates that the defect formation energy depends on the chemical potentials of the atomic species, which are determined by the experimental growth conditions and can be either Zn-rich, O-rich, or anything in between. These chemical potentials are limited by the formation of bulk ZnO and Al_2O_3 through the thermodynamic stability condition. For instance, Zn-rich (O-poor) conditions place an upper limit on μ_{Zn} by $\mu_{Zn}=E[Zn_{bulk}]$. This upper limit for zinc leads to a lower limit on μ_O given by the thermodynamic stability condition for ZnO : $\mu_O=E[O_2]/2 + \Delta H_f[ZnO]$, with $\Delta H_f[ZnO]$=-3.12eV the enthalpy of formation of bulk ZnO. As a result μ_{Al} is $\mu_{Al}=E[Al_{bulk}] + \Delta H_f[Al_2O_3]/2 - 3\Delta H_f[ZnO]/2$, with $\Delta H_f[Al_2O_3]$=-17.19 eV the enthalpy of formation of bulk Al_2O_3.

RESULTS AND DISCUSSIONS

ICP-AES results show that the dopant concentration in the acquired powders is 0.45 mol% for both the as-synthesized and annealed samples. This means that the dopant concentration does not change during the annealing procedure. XRD analysis (not shown) confirmed that both powders were of wurtzite structure, and no side phases were present. TEM micrographs are shown in Figure 1 and indicate that quasi-spherical elongated particles were obtained after synthesis, with a narrow size distribution, which does not change after annealing.

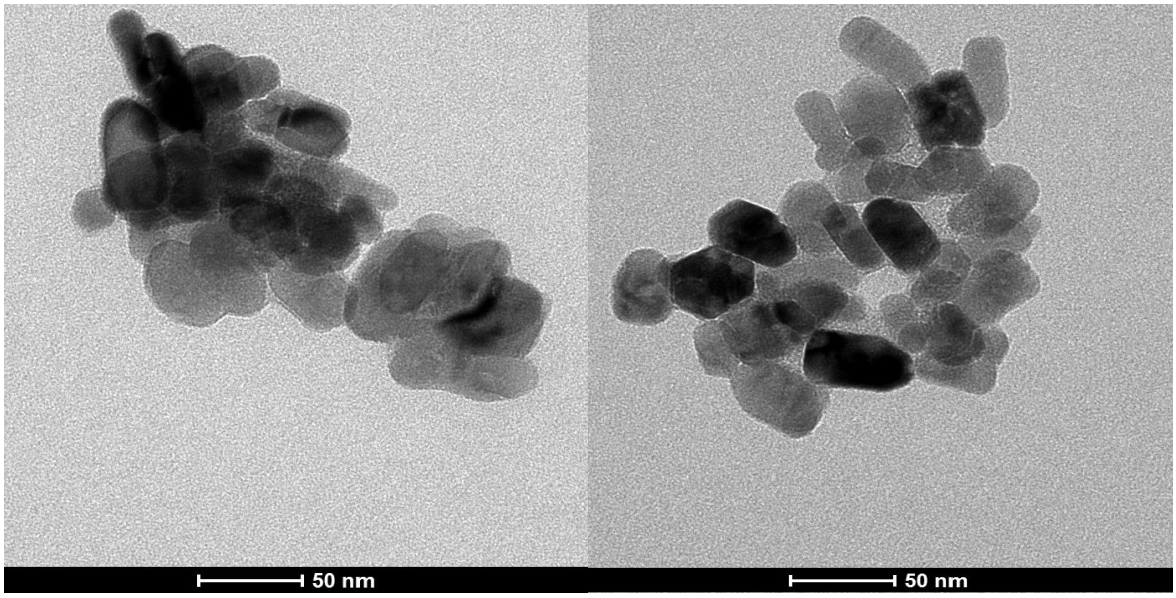

Figure 1. TEM images of ZnO:Al nanoparticles. Left: before anneal. Right: after annealing.

The particles appear to be about 40 nm in size, and no secondary phase is observed in electron diffraction nor bright field images. FT-IR spectra presented in Figure 2 show an absorption band around 400-500 cm^{-1} which can be attributed to the Zn-O stretching mode, and a broad band around 3500 cm^{-1}, attributed to adsorbed water as reported in other studies [63]. No signals corresponding to organic materials are identified. Both spectra indicate the presence of free charge carriers as identified by the surface plasmon resonance (SPR) absorption band located between 600 and 3000 cm^{-1} [10]. We observe this band immediately

after synthesis, indicating that shallow donors are already present in the as-synthesized samples.

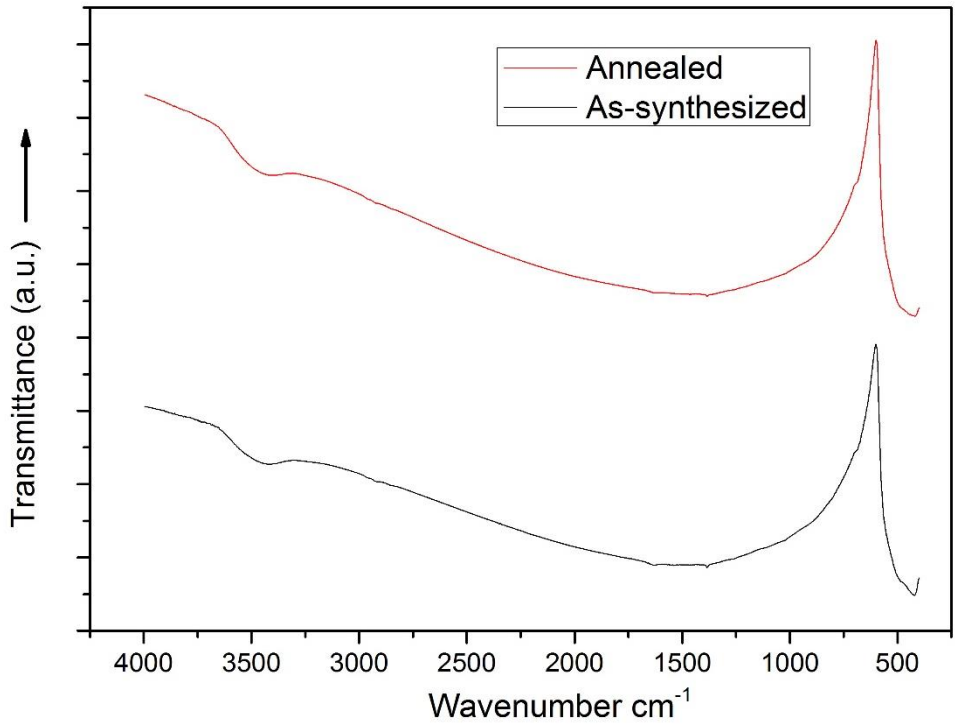

Figure 2. FT-IR spectra of as-synthesized (bottom) and annealed (top).

In order to attain semi-quantitative information on the conductivity of the nanoparticles, MCPT measurements, shown in Figure 3, were carried out that determine the complex permittivity of the sample. For reference purposes, also MCPT measurements were performed for pure ZnO samples in the same way as for ZnO:Al samples. The results are listed in Table 1 and demonstrate that as-synthesized AZO samples have a higher imaginary permittivity ε'' than pure ZnO samples due to doping with Al, corresponding to a higher sample conductivity as given by $\varepsilon'' = \sigma/\varepsilon_0\omega$, where σ is the conductivity of the AZO, ε_0 is the permittivity of free space and ω is the angular frequency at which the sample is measured [64]. Annealed ZnO and AZO samples have higher imaginary permittivity, compared

to as-synthesized samples, but a much higher imaginary permittivity is obtained in the AZO samples.

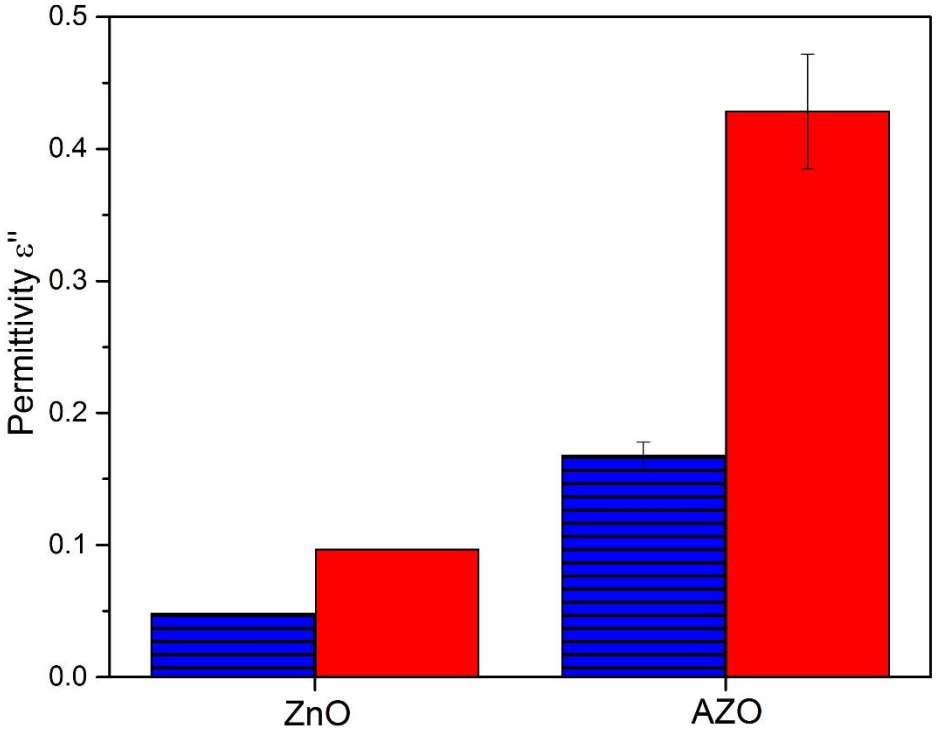

Figure 3. MCPT measurements result at 2.4GHz. Blue (horizontal lines) - as-synthesized, red (empty) – annealed, with standard deviation bars.

Table 1. MCPT measurements results.

SAMPLE	PERMITTIVITY AS-SYNTHESYZED	PERMITTIVITY AFTER ANNEAL
PURE ZnO	0.05	0.10
AZO	0.17 (±0.01)	0.43 (±0.04)

Next, the AZO and pure ZnO samples (the as-synthesized as well as the annealed ones) were characterized by Raman spectroscopy. The measured Raman modes shown in Figure 4 and 5 are assigned based on a study by Russo [44]. For ease of interpretation, the Raman spectra were first normalized with respect to the E_2^{Low} peak, which is attributed to the zinc

sublattice. First, we consider the Raman measurement results for the AZO samples in Figure 4. After annealing, there is a decrease in intensity of the E_2^{high} peak, and simultaneous increase in intensity of E_1(LO) peak. The ratio between two peaks is associated with the amount of oxygen vacancies in the lattice[44]. After de-convolution (Supplementary data S1 and S2) the ratios of peaks E_2^{high} to E_1(LO) are 2.42 for the as-synthesized sample, and 1.87 for the annealed sample, indicating increased amount of oxygen vacancies. Indeed, a change of color is observed from white to yellow in the annealed samples, usually associated with oxygen vacancies that form under nitrogen rich conditions [65, 66]. These results confirm that the oxygen sub-lattice is more sensitive to the annealing conditions than the zinc sub-lattice [44]. The mode detected at 500 cm^{-1} exhibits A_1 symmetry and is assigned to longitudinal acoustical (LA) overtones [67]. The spectrum also shows an anomalous mode (AM) at 275 cm^{-1} that, according to Gluba et al. [24], is related to interstitial zinc clusters, in which the contributing Zn atoms are located in neighbouring interstitial sites.

These authors speculate that such clusters might be responsible for unintentional zinc oxide n-type conductivity. In this work, the intensity of this AM is seen to increase after annealing, which indicates that the amount of zinc interstitials is increased. Also, it is evident that the signal to noise ratio decreases after annealing, meaning that the crystallinity of the sample decreases, which we link to the increased number of oxygen vacancies. The increase in oxygen vacancies after annealing, should lead to oxygen interstitials, which are electron traps in an n-type material. Nevertheless, the MCPT measurements indicated an increase in conductivity associated with the measured imaginary permittivity, so the overall effect of the annealing procedure is still a strong increase in free charge carriers.

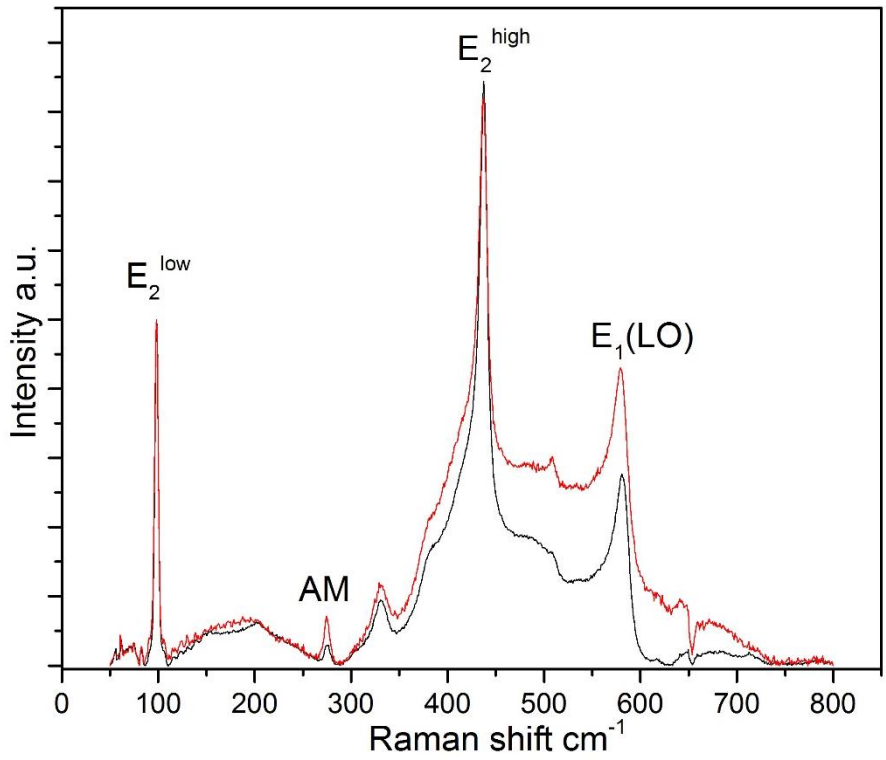

Figure 4. Raman spectra of aluminum doped zinc oxide, as-synthesized (black) and after annealing (red). After annealing, increase of oxygen vacancies (E2 high decreases), and increase of Zn interstitial clusters (AM) is shown. Spectra have been normalized based on the E_2^{low} peak.

The change in intensity of the E_2^{high} mode in the case of pure ZnO, as shown in Figure 5, is much less pronounced compared to AZO. This might indicate that there are less oxygen vacancies created during the annealing of the pure ZnO sample, on the other hand it might be that the presence of aluminum in the AZO sample has an influence on the signal strength of this mode.

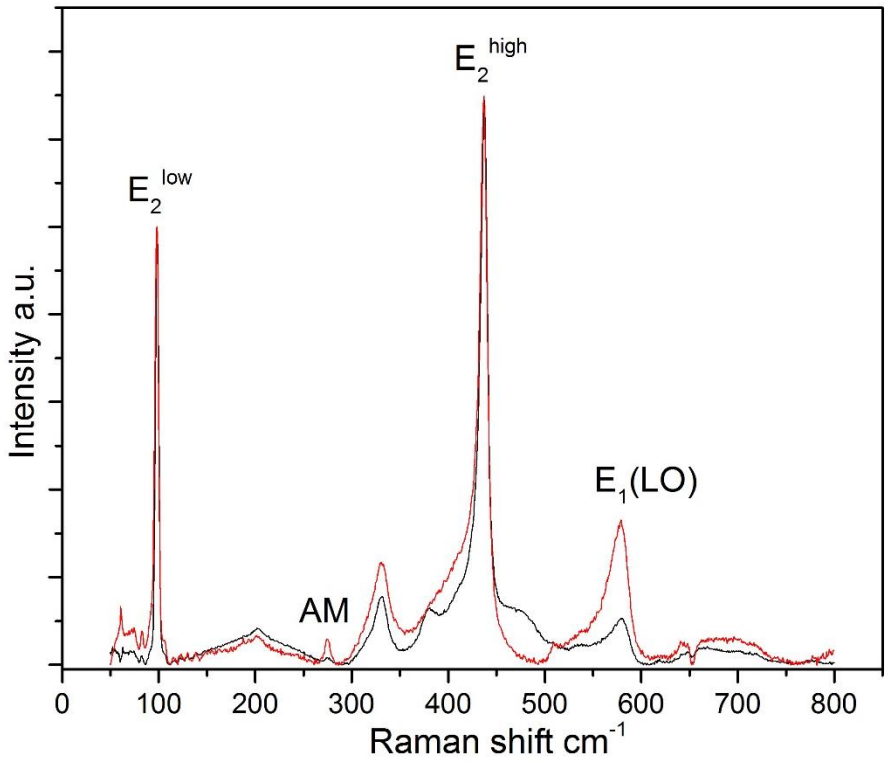

Figure 5.Raman spectra of pure zinc oxide. As-synthesized (black) and after annealing (red).

With the Al^{27}-NMR technique, the oxygen coordination of the Al atoms in ZnO can be determined. Therefore the technique is widely used to study the position of aluminum in the crystalline lattice [68-70]. We use it to determine the influence of annealing on the migration of aluminum. From the spectrum for the as-synthesized AZO sample, shown in Figure 6 (left figure), we observe that most of the aluminum atoms are in the octahedral position (corresponding to the peak at 15 ppm), and a smaller fraction of the aluminum atoms is in a tetrahedral position (corresponding to the peak around 80 ppm)[71]. One can also observe a peak at 188 ppm. At this position, the side band of the octahedral peak can be expected, but it can also be a weak knight shift (KS) signal. In this case, we have two indications to fully attribute the peak at 188 ppm to a side band of the octahedral aluminum peak. First, because we observe such a strong peak at 15 ppm related to the octahedrally coordinated Al atoms, a significant side band can indeed be expected [72]. Second, the shape of the observed peak at 188 ppm, is typical for a side band. From the area under the NMR

peaks, we deduce that 80 % of the Al atoms is in an octahedral interstitial position before annealing. To be able to distinguish between Al atoms in substitutional or interstitial tetrahedral positions, T_1 relaxation measurements were carried out [28, 30]. From the results, presented in Table 2, it is evident that the amount of substitutional Al with a long decaying time of 2.7 seconds in as-synthesized powders is as low as 5%, while there is 15% of the total Al atoms in an interstitial tetrahedral position with a decay time as short as 0,035 s.

From the NMR spectrum for the annealed sample shown in Figure 6 (right figure) it is clear that most aluminum atoms change their position into a tetrahedral position after annealing. Remarkably, also the peak at 188 ppm has increased significantly in intensity. Since the signal of octahedral Al has become now rather small, its side band should not interfere with the KS signal.

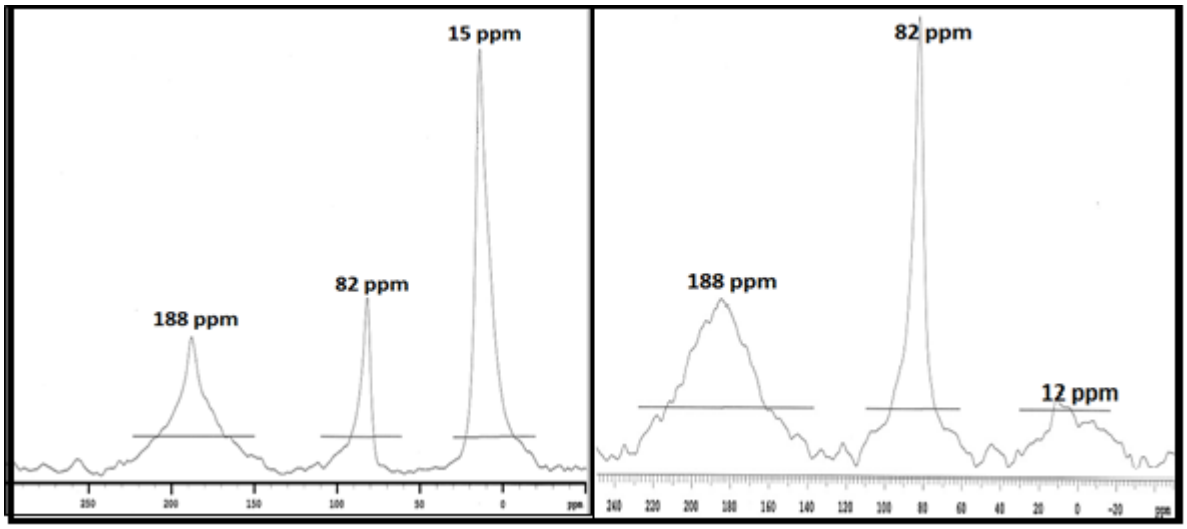

Figure 6. NMR spectra of aluminium doped zinc oxide. As-synthesized (left) and after annealing (right).

Also notable is the change in peak shape with respect to the as-synthesized case. Therefore, we interpret this peak at 188 ppm for the annealed sample as a KS peak and include it in the determination/quantification of the different Al fractions (Table 2). Considering again the

area under the Raman peaks together with T_1 relaxation time measurements, we find that in the annealed sample the amount of substitutional Al increases up to 22%, while the interstitial tetrahedral Al decreases down to 10%. Also the amount of interstitial Al at the octahedral position decreases down to 10% of the total Al atoms. Also a much stronger KS signal can be seen, which accounts for 58% of the total number of Al atoms. Typically, such KS signal is associated with Al in the close neighbourhood to some extended, mobile electrons [73]. The assignment of this KS to metallic aluminium in the sample can be excluded, as literature states that the KS signal of the metallic state should appear at much higher ppm (namely around 1640 ppm) [74] than in the current case. Also, previous studies have not found any evidence for the presence of metallic zinc or aluminum in AZO even after a reductive annealing [43]. Such a KS peak was also never observed in as-synthesized samples with a large amount of substitutional Al atoms. Therefore its origin must lie in the way substitutional Al atoms were created upon annealing. As an interstitial Al atom that migrates to a substitutional position must also create a Zn interstitial, our experimental observations suggest that the KS signal originates from substitutional Al atoms with Zn interstitials in their close neighbourhood, which are then responsible for the extended, mobile electrons around the substitutional Al. Attributing the KS signal to Al_{Zn}, we find that almost 80% of Al is now in a substitutional position.

Table 2.Results of ^{27}Al NMR T_1 measurements corresponding peak-area fraction before annealing, and after annealing taking into account KS area

	Al_{Oh}/T1(s)	Al_{Th}/T1(s)	Al_{Zn}/T1(s)
As-synthesized	80%/1.05	15%/0.035	5%/2.7
Annealed (incl. KS)	12%/-	12%/0.088	24%/6.69+52%(KS)/0.56

Thus, NMR and Raman spectra suggest that during annealing, interstitial Al_i moves to the substitutional position and the amount of interstitial Zn increases, coinciding with an

enhanced conductivity, as measured by the MCPT measurements. Isolated substitutional Al as well as interstitial Zn are both shallow donors, substitutional Al in the 1+ charge state, Zn interstitial in the 2+ charge state. Therefore, it might be questionable if such two shallow donors can be created close to each other. This transition can only occur if it leads to a more stable state (thermodynamic aspect) and has a reasonable energy barrier (kinetic aspect). Therefore, to support the interpretation of the experimental data, we performed first-principles calculations to assess the defect type, charge state and formation energy of the Al interstitial defects, both at the octahedral (Al_{Oh}) and the tetrahedral (Al_{Th}) position, and the complex of a substitutional Al atom with a Zn interstitial close to it (Al_{Zn}-Zn_i). As the created Zn interstitials might migrate, also the Zn_i-Zn_i complex is considered.

Figure 7 presents our hybrid functional based defect formation energies, including the tetrahedral as well as octahedral Al_i in the ZnO supercell as a function of the Fermi level E_F. The calculations are performed considering a bulk-like system, since the TEM results indicate that the particles have a width of approximately 40 nm which is large enough to show ZnO bulk characteristics. Both interstitials act as shallow donors and are in the 1+ charge state for Fermi levels close to the conduction band. So we predict that the Al interstitial provides one charge carrier in n-type ZnO, and not three, as claimed in[31]. The tetrahedral interstitial has a slightly lower formation energy. For completeness, Figure 7 also shows that Al_{Zn} has a much lower formation energy for Fermi levels close to the conduction band, and, as expected, acts as a shallow donor that contributes one electron to the charge carriers in ZnO.

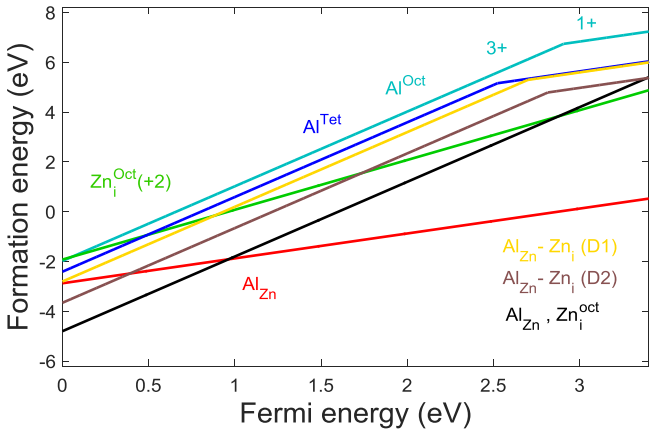

Figure 7. Calculated formation energies as a function of Fermi energy for several defects in ZnO under O-poor conditions.

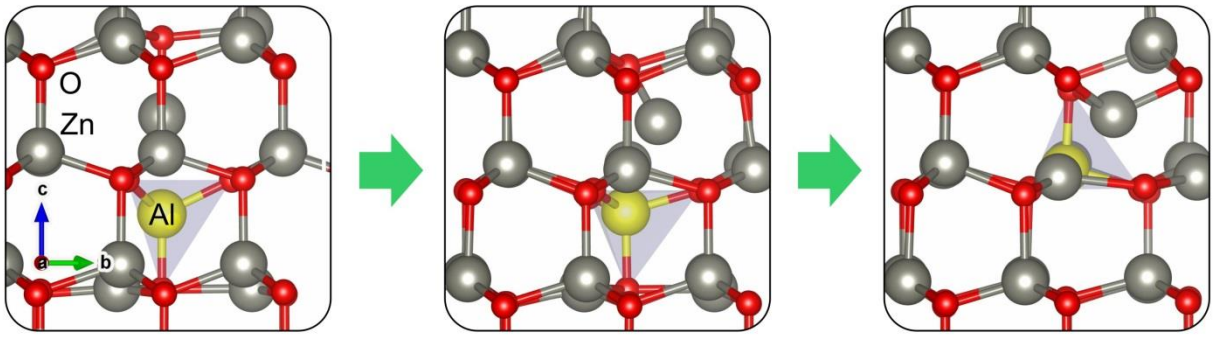

Figure 8. The structural transition from the relaxed Al defect towards the Al_{Zn}-Zn_i complex, all in the 1+ charge state.

Our experimental results suggest that an interstitial Al_i can move to a substitutional position by pushing away a Zn atom that becomes a Zn_i. It is known that an isolated Zn_i occupies an octahedral position and behaves as a shallow donor in charge state 2+, which is also confirmed by our hybrid functional first-principles calculations as shown in Figure 7. This would result in two shallow donors, next to each other, which could lead to a large Coulomb repulsion, and thus a high energy configuration. Therefore we compared the formation energy of the Al_{Zn}-Zn_i complex with that of the interstitial Al_i. The obtained results in Figure 7 show that the Al_{Zn}-Zn_i complex in ZnO in which Zn_i is located in the "cage" next to Al_{Zn}

(called configuration D1) has a lower formation energy than the interstitial Al_i and is stable in the 1+ charge state. This confirms that the complex is indeed energetically favored over the isolated interstitial defects. The distance between the Al_{Zn} and Zn_i dopants in this D1 configuration is 2.57 Å. When the Zn_i is moved one "cage" further away (into configuration called D2), this distance increases to 4.37 Å, and the energy is reduced. Figure 7 also shows the sum of the formation energies of both isolated Al_{Zn} and Zn_i defects, corresponding to two infinitely separated defects, further reducing the energy.

To gain more insight in this transition and in the required energy barrier, we used the nudged elastic band (NEB) method to calculate the path between the interstitial Al_i and the Al_{Zn}-Zn_i complex. These calculations are done with the PBE functional to reduce the computational cost, as similar results can be expected for the hybrid functional [75, 76]. Figure 8 shows the relaxed start configuration around the Al_{Td}, the relaxed end configuration of the Al_{Zn}-Zn_i complex (which we called the D1 configuration), and an intermediate structure, all in the 1+ charge state. Note that the interstitial Al is indeed tetrahedrally coordinated by four oxygen atoms, but that also a nearby Zn atom is already considerably pushed away from its equilibrium position (the Zn atom has moved a distance of 1.17 Å for the system in the 1+ charge state with respect to its position in a pure ZnO system). It is therefore also not surprising that it is indeed possible that the Al_{Td} can push the Zn atom further away. Figure 9(a) shows the total energies for some intermediate configurations between the initial Al_{Td} and final Al_{Zn}-Zn_i complex obtained by the NEB method, for the 1+ charge state. The initial energy barrier is very small. A local minimum is reached at structure 6. This is the point where the Al atom reaches the substitutional position and the interstitial Zn atom the

octahedral position in the middle of the "cage". Finally the Zn atom has to overcome an extra barrier of ~ 0.1 eV in order to reach the final Al_{Zn}-Zn_i structure.

We performed a similar study with the NEB method to calculate the path of the transition between the Al_{Oh} dopant and the Al_{Zn}-Zn_i complex. Figure 9(b) shows total energies for some configurations along this path for the system, again in the 1+ charge state. It is clear that now a much higher barrier of ~0.53 eV has to be overcome. After this barrier, the same path as for the Al_{Td} is followed, which shows that the Al_{Oh} first moves to Al_{Td} position before it converts to the Al_{Zn}-Zn_i complex. Based on the temperature dependent measured diffusion coefficient of Al in ZnO [77], we estimate the diffusion constant to be

$$\mathrm{D} = 5.3 \times 10^{-2}\ cm^2 s^{-1} \exp\left(-\frac{E_a}{k_B T}\right), \qquad (2)$$

with E_a the energy barrier and k_B Boltzmann's constant. An annealing temperature of 400°C, energy barriers of the order of 0.53 eV, lead to a diffusion coefficient of $5.72 \times 10^{-6}\ cm^2 s^{-1}$. The barrier is thus not too high

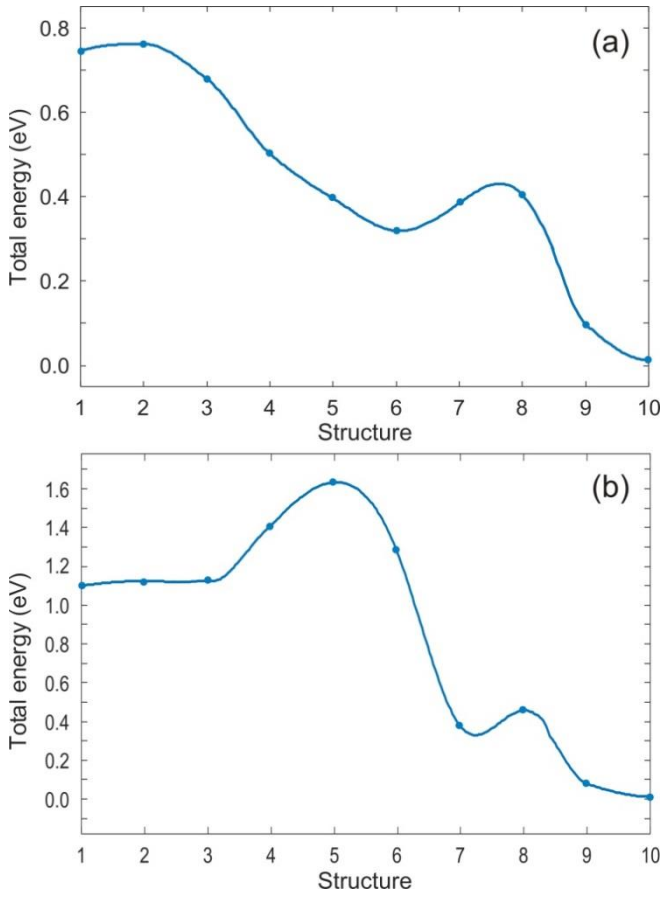

Figure 9. Barrier energy between (a) Al_{Td} and (b) Al_{Oh} dopants and the Al_{Zn}-Zn_i complex in ZnO, system in the 1+ charge state.

While an isolated substitutional Al atom is in the 1+ charge state, and an isolated Zn interstitial in the 2+ charge state, the Al_{Zn}-Zn_i complex is in the 1+ state for Fermi levels close to the conduction band. This is caused by the interaction between two atomic defect levels located in the conduction band of ZnO that interact and form an occupied bonding level with an energy located in the band gap. The density of these two bonding levels in the Al_{Zn}-Zn_i complex is shown in Figure 10. Isolated substitutional Al atoms were never observed to lead to a KS signal. However, in our samples the substitutional atoms are created mainly after annealing, which thus also includes the creation of Zn interstitials. Therefore, we attribute the observed KS signal to the presence of these extra bonding electrons interacting with the substitutional Al atoms.

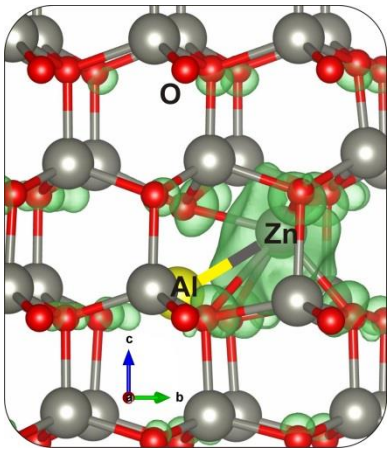

Figure 10. Density of the bonding in the Al_{Zn}-Zn_i complex.

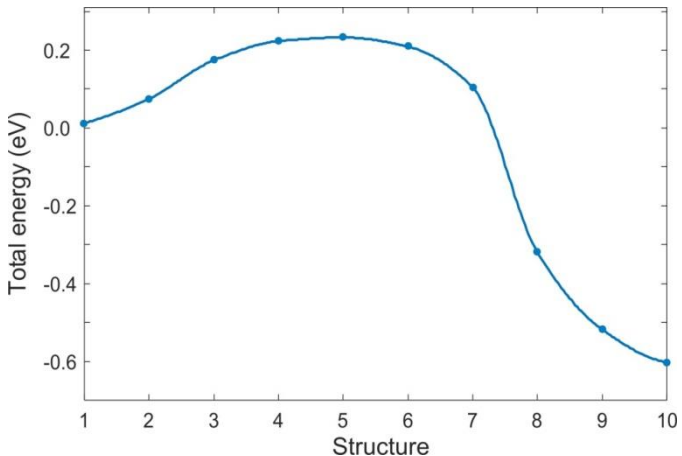

Figure 11. Barrier energy between Al_{Zn}-Zn_i (D1) *complex and the* Al_{Zn}-Zn_i (D2) *complex in ZnO, system in the 1+ charge state.*

As mentioned above, the Al_{Zn}-Zn_i complex in the D1 configuration is not the lowest energy state. If the Zn_i moves one cage further, the energy decreases with approximately 0.61 eV. The NEB calculation for this transition, shown in Figure 11, indicates that an energy barrier of ~0.2 eV has to be overcome in this transition. Finally the Zn interstitial can become an isolated defect, in the 2+ charge state. If this happens, the total number of charge carriers has increased from 1 to 3 by going from the interstitial Al to the isolated substitutional Al atom and Zn interstitial.

Additional experiments have shown, that after prolonged anneal the KS signal (188ppm) loses its intensity. This indicates that after prolonged anneal a Zn interstitial can become an isolated defect, migrating away from the Al substitutional. However, as shown is Figure 12, this process is not instantaneous, since even after two hour anneal at 400°C in nitrogen, the KS signal still can be clearly seen, although substantially smaller.

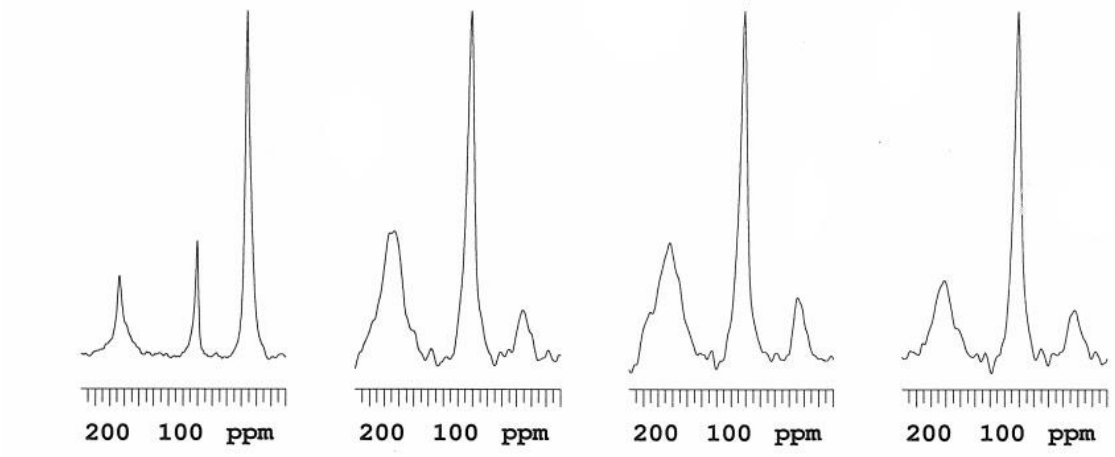

Figure 12. NMR spectra of AZO. Left to right: as-synthesized, 10min anneal, 30min anneal, 2 hour anneal.

Another possibility is that the Zn interstitials form a cluster, which might lead to a more thermally stable defect. Figure 13 shows the formation energies for different charge states

of such a Zn_i-Zn_i cluster in ZnO. For Fermi levels close to the conduction band, the 2+ charge state of the Zn_i-Zn_i cluster is the most stable charge, similar to the conclusions obtained in [24] based on calculations for the neutral Zn_i-Zn_i cluster. Also note that the total formation energy is lower than the formation energy of two independent Zn_i defects, which is also shown in Figure 12 (it is just twice the formation energy of the Zn_i defect shown in Figure 7). In such a Zn_i-Zn_i cluster, the Zn [$4s^2$] orbitals create a bonding (Zn_2 σ) and an antibonding (Zn_2 σ*) orbital which are fully occupied. The σ orbital hybridizes with O [2p] orbitals in ZnO forming a bonding (Zn_2 σ+ O 2p) and an antibonding (Zn_2 σ+ O 2p)* orbital. The antibonding (Zn_2 σ*) orbital which is located in the conduction band transfers two electrons to the conduction band minimum and yields a shallow donor complex [24]. Again the total number of charge carriers has increased with respect to the initial interstitial situation.

Figure 13. Calculated formation energies as a function of Fermi energy for different charge states of $Zn_i - Zn_i$ cluster in ZnO (blue line). For completeness also the formation energy of a single (green line) and two non-interacting Zni defects (dotted red line) are shown. All results are for O-poor conditions.

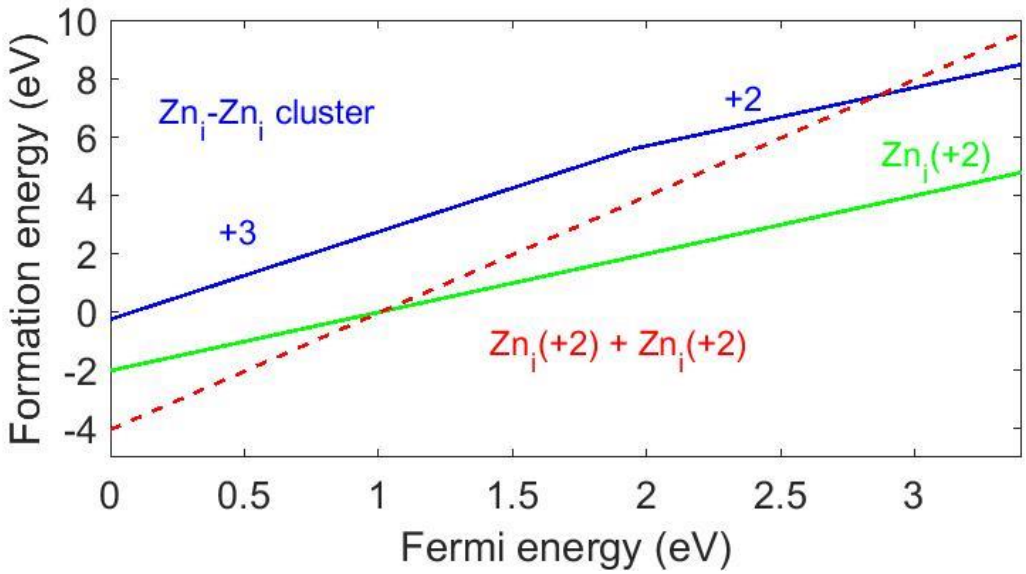

CONCLUSIONS

A combined study involving an experimental and theoretical approach has been carried out to gain better understanding of the effect of annealing on aluminum doped zinc oxide nanoparticles. Analysis has shown that during the annealing there is a significant migration of aluminum from interstitial positions into the substitutional position, accompanied by the creation of zinc interstitials. Our first-principles calculations indeed show that the transition from an Al interstital towards a substitutional position together with the creation of a zinc interstitial lowers the defect energy. The charge state of the Al interstitial as well as of the Al_{Zn}-Zn_i complex is both 1+, for Fermi levels close to the conduction band minimum. When the zinc interstitial migrates further away, its charge state turns into 2+. Also Zn clusters can be formed. In both cases the number of charge carriers has increased with respect to the Al interstitial, explaining the increased conductivity. Further, after annealing, a Knight shifted peak in ^{27}Al NMR is observed. Our combined experimental and theoretical study suggests that this signal originates from substitutional Al atoms with such Zn interstitials in their close neighbourhood, which are then responsible for the extended, mobile electrons around the substitutional Al.

ACKNOWLEDGEMENTS

We want to thank the Interuniversity Attraction Poles Programme (P7/05) initiated by the Belgian Science Policy Office (BELSPO) for the financial support. We also acknowledge the Research Foundation Flanders (FWO-Vlaanderen) for support via the MULTIMAR WOG project and under project No. G018914.

The computational parts were carried out using the HPC infrastructure at the University of Antwerp (CalcUA), a division of the Flemish Supercomputer Center VSC, supported financially by the Hercules foundation and the Flemish Government (EWI Department).

REFERENCES

1. Janotti, A.; Van de Walle, C. G., Fundamentals of zinc oxide as a semiconductor. *Reports on Progress in Physics* **2009,** 72, (12), 126501.
2. Özgür, U.; Alivov, Y. I.; Liu, C.; Teke, A.; Reshchikov, M. A.; Doğan, S.; Avrutin, V.; Cho, S. J.; Morkoç, H., A comprehensive review of ZnO materials and devices. *Journal of Applied Physics* **2005,** 98, (4), 041301.
3. Wang, Z. L., Zinc oxide nanostructures: growth, properties and applications. *Journal of Physics: Condensed Matter* **2004,** 16, (25), R829-R858.
4. Schmidt-Mende, L.; MacManus-Driscoll, J. L., ZnO – nanostructures, defects, and devices. *Materials Today* **2007,** 10, (5), 40-48.
5. Kakiuchi, K.; Hosono, E.; Fujihara, S., Enhanced photoelectrochemical performance of ZnO electrodes sensitized with N-719. *Journal of Photochemistry and Photobiology A: Chemistry* **2006,** 179, (1-2), 81-86.
6. Yadav, A.; Prasad, V.; Kathe, A. A.; Raj, S.; Yadav, D.; Sundaramoorthy, C.; Vigneshwaran, N., Functional finishing in cotton fabrics using zinc oxide nanoparticles. *Bulletin of Materials Science* **2006,** 29, (6), 641-645.
7. Tien, L. C.; Sadik, P. W.; Norton, D. P.; Voss, L. F.; Pearton, S. J.; Wang, H. T.; Kang, B. S.; Ren, F.; Jun, J.; Lin, J., Hydrogen sensing at room temperature with Pt-coated ZnO thin films and nanorods. *Applied Physics Letters* **2005,** 87, (22), 222106.
8. Bian, J.; Luo, Y.; Sun, J.; Liang, H.; Liu, W.; Hu, L., Synthesis and temperature dependent photoluminescence of Zn1−x Mg x O films grown by ultrasonic spray pyrolysis. *Journal of Materials Science* **2007,** 42, (20), 8461-8464.
9. Serier, H.; Gaudon, M.; Ménétrier, M., Al-doped ZnO powdered materials: Al solubility limit and IR absorption properties. *Solid State Sciences* **2009,** 11, (7), 1192-1197.
10. Buonsanti, R.; Llordes, A.; Aloni, S.; Helms, B. A.; Milliron, D. J., Tunable infrared absorption and visible transparency of colloidal aluminum-doped zinc oxide nanocrystals. *Nano Lett* **2011,** 11, (11), 4706-4710.
11. Fernández, S.; Naranjo, F. B., Optimization of aluminum-doped zinc oxide films deposited at low temperature by radio-frequency sputtering on flexible substrates for solar cell applications. *Solar Energy Materials and Solar Cells* **2010,** 94, (2), 157-163.
12. Guillén, C.; Herrero, J., Optical, electrical and structural characteristics of Al:ZnO thin films with various thicknesses deposited by DC sputtering at room temperature and annealed in air or vacuum. *Vacuum* **2010,** 84, (7), 924-929.
13. Hartner, S.; Ali, M.; Schulz, C.; Winterer, M.; Wiggers, H., Electrical properties of aluminum-doped zinc oxide (AZO) nanoparticles synthesized by chemical vapor synthesis. *Nanotechnology* **2009,** 20, (44), 445701.
14. Jiang, X.; Wong, F. L.; Fung, M. K.; Lee, S. T., Aluminum-doped zinc oxide films as transparent conductive electrode for organic light-emitting devices. *Applied Physics Letters* **2003,** 83, (9), 1875-1877.
15. Suchea, M.; Christoulakis, S.; Katsarakis, N.; Kitsopoulos, T.; Kiriakidis, G., Comparative study of zinc oxide and aluminum doped zinc oxide transparent thin films grown by direct current magnetron sputtering. *Thin Solid Films* **2007,** 515, (16), 6562-6566.
16. Rusop, M.; Uma, K.; Soga, T.; Jimbo, T., Post-growth annealing of zinc oxide thin films pulsed laser deposited under enhanced oxygen pressure on quartz and silicon substrates. *Materials Science and Engineering: B* **2006,** 127, (2–3), 150-153.
17. Pak, C. M.; Su, S. C.; Ling, C. C.; Lu, Y. M.; Zhu, D. L., Post-growth annealing study of heavily Ga-doped zinc oxide grown by radio frequency magnetron sputtering. *Journal of Physics D: Applied Physics* **2013,** 46, (13), 135104.
18. Xing, G. Z.; Yao, B.; Cong, C. X.; Yang, T.; Xie, Y. P.; Li, B. H.; Shen, D. Z., Effect of annealing on conductivity behavior of undoped zinc oxide prepared by rf magnetron sputtering. *Journal of Alloys and Compounds* **2008,** 457, (1–2), 36-41.

19. Ng, Z.-N.; Chan, K.-Y.; Tohsophon, T., Effects of annealing temperature on ZnO and AZO films prepared by sol–gel technique. *Applied Surface Science* **2012,** 258, (24), 9604-9609.
20. Zhang, C. Y., The influence of post-growth annealing on optical and electrical properties of p-type ZnO films. *Materials Science in Semiconductor Processing* **2007,** 10, (4–5), 215-221.
21. Vinodkumar, R.; Lethy, K. J.; Beena, D.; Satyanarayana, M.; Jayasree, R. S.; Ganesan, V.; Nayar, V. U.; Mahadevan Pillai, V. P., Effect of thermal annealing on the structural and optical properties of nanostructured zinc oxide thin films prepared by pulsed laser ablation. *Solar Energy Materials and Solar Cells* **2009,** 93, (1), 74-78.
22. Lupan, O.; Pauporté, T.; Chow, L.; Viana, B.; Pellé, F.; Ono, L. K.; Roldan Cuenya, B.; Heinrich, H., Effects of annealing on properties of ZnO thin films prepared by electrochemical deposition in chloride medium. *Applied Surface Science* **2010,** 256, (6), 1895-1907.
23. Lee, C.; Lee, W.; Kim, H.; Kim, H. W., Influence of annealing atmosphere on the structure, resistivity and transmittance of InZnO thin films. *Ceramics International* **2008,** 34, (4), 1089-1092.
24. Gluba, M. A.; Nickel, N. H.; Karpensky, N., Interstitial zinc clusters in zinc oxide. *Physical Review B* **2013,** 88, (24), 245201.
25. Janotti, A.; Van de Walle, C. G., Native point defects in ZnO. *Physical Review B* **2007,** 76, (16), 165502.
26. Van de Walle, C. G., Hydrogen as a Cause of Doping in Zinc Oxide. *Physical Review Letters* **2000,** 85, (5), 1012-1015.
27. Janotti, A.; Van de Walle, C. G., Oxygen vacancies in ZnO. *Applied Physics Letters* **2005,** 87, (12), 122102.
28. Avadhut, Y. S.; Weber, J.; Hammarberg, E.; Feldmann, C.; Schmedt auf der Gunne, J., Structural investigation of aluminium doped ZnO nanoparticles by solid-state NMR spectroscopy. *Phys Chem Chem Phys* **2012,** 14, (33), 11610-25.
29. Saniz, R.; Xu, Y.; Matsubara, M.; Amini, M. N.; Dixit, H.; Lamoen, D.; Partoens, B., A simplified approach to the band gap correction of defect formation energies: Al, Ga, and In-doped ZnO. *Journal of Physics and Chemistry of Solids* **2013,** 74, (1), 45-50.
30. Kemmitt, T.; Ingham, B.; Linklater, R., Optimization of Sol–Gel-Formed ZnO:Al Processing Parameters by Observation of Dopant Ion Location Using Solid-State27Al NMR Spectrometry. *The Journal of Physical Chemistry C* **2011,** 115, (30), 15031-15039.
31. Johansen, K. M.; Vines, L.; Bjørheim, T. S.; Schifano, R.; Svensson, B. G., Aluminum Migration and Intrinsic Defect Interaction in Single-Crystal Zinc Oxide. *Physical Review Applied* **2015,** 3, (2), 024003.
32. Calnan, S.; Riedel, W.; Gledhill, S.; Stannowski, B.; Schlatmann, R.; Lux-Steiner, M. C., Zinc oxide films grown by galvanic deposition from 99% metals basis zinc nitrate electrolyte. *Journal of Materials Chemistry A* **2014,** 2, (25), 9626.
33. Kaida, T.; Kamioka, K.; Ida, T.; Kuriyama, K.; Kushida, K.; Kinomura, A., Rutherford backscattering and nuclear reaction analyses of hydrogen ion-implanted ZnO bulk single crystals. *Nuclear Instruments and Methods in Physics Research Section B: Beam Interactions with Materials and Atoms* **2014,** 332, 15-18.
34. Chen, Z. Q.; Yamamoto, S.; Maekawa, M.; Kawasuso, A.; Yuan, X. L.; Sekiguchi, T., Postgrowth annealing of defects in ZnO studied by positron annihilation, x-ray diffraction, Rutherford backscattering, cathodoluminescence, and Hall measurements. *Journal of Applied Physics* **2003,** 94, (8), 4807.
35. Lv, J.; Li, C.; BelBruno, J. J., Characteristics of point defects on the optical properties of ZnO: revealed by Al–H co-doping and post-annealing. *RSC Advances* **2013,** 3, (23), 8652.
36. Rodrigo Noriega, L. G. J. R. J. S. L. M. T. A. C. P. J. F. S. A. S., Transport and structural characterization of solution-processable doped ZnO nanowires. *Proc.SPIE* **2009,** 7411, 7411 - 7411 - 6.
37. Oga, T.; Izawa, Y.; Kuriyama, K.; Kushida, K.; Kinomura, A., Origins of low resistivity in Al ion-implanted ZnO bulk single crystals. *Journal of Applied Physics* **2011,** 109, (12), 123702.

38. Roberts, N.; Wang, R. P.; Sleight, A. W.; Warren, W. W., ^{27}Al and ^{69}Ga impurity nuclear magnetic resonance in ZnO:Al and ZnO:Ga. *Physical Review B* **1998,** 57, (10), 5734-5741.
39. Knight, W. D., Nuclear Magnetic Resonance Shift in Metals. *Physical Review* **1949,** 76, (8), 1259-1260.
40. Townes, C. H.; Herring, C.; Knight, W. D., The Effect of Electronic Paramagnetism on Nuclear Magnetic Resonance Frequencies in Metals. *Physical Review* **1950,** 77, (6), 852-853.
41. Kelchtermans, A.; Adriaensens, P.; Slocombe, D.; Kuznetsov, V. L.; Hadermann, J.; Riskin, A.; Elen, K.; Edwards, P. P.; Hardy, A.; Van Bael, M. K., Increasing the Solubility Limit for Tetrahedral Aluminium in ZnO:Al Nanorods by Variation in Synthesis Parameters. *Journal of Nanomaterials* **2015,** 2015, 1-8.
42. Kelchtermans, A.; Elen, K.; Schellens, K.; Conings, B.; Damm, H.; Boyen, H.-G.; D'Haen, J.; Adriaensens, P.; Hardy, A.; Van Bael, M. K., Relation between synthesis conditions, dopant position and charge carriers in aluminium-doped ZnO nanoparticles. *RSC Advances* **2013,** 3, (35), 15254.
43. Damm, H.; Adriaensens, P.; De Dobbelaere, C.; Capon, B.; Elen, K.; Drijkoningen, J.; Conings, B.; Manca, J. V.; D'Haen, J.; Detavernier, C.; Magusin, P. C. M. M.; Hadermann, J.; Hardy, A.; Van Bael, M. K., Factors Influencing the Conductivity of Aqueous Sol(ution)–Gel-Processed Al-Doped ZnO Films. *Chemistry of Materials* **2014,** 26, (20), 5839-5851.
44. Russo, V.; Ghidelli, M.; Gondoni, P.; Casari, C. S.; Li Bassi, A., Multi-wavelength Raman scattering of nanostructured Al-doped zinc oxide. *Journal of Applied Physics* **2014,** 115, (7), 073508.
45. Slocombe, D.; Porch, A.; Bustarret, E.; Williams, O. A., Microwave properties of nanodiamond particles. *Applied Physics Letters* **2013,** 102, (24), 244102.
46. Perdew, J. P.; Burke, K.; Ernzerhof, M., Generalized Gradient Approximation Made Simple. *Physical Review Letters* **1996,** 77, (18), 3865-3868.
47. Heyd, J.; Scuseria, G. E.; Ernzerhof, M., Hybrid functionals based on a screened Coulomb potential. *The Journal of Chemical Physics* **2003,** 118, (18), 8207-8215.
48. Kresse, G.; Furthmüller, J., Efficient iterative schemes for ab initio total-energy calculations using a plane-wave basis set. *Physical Review B* **1996,** 54, (16), 11169-11186.
49. Kresse, G.; Furthmüller, J., Efficiency of ab-initio total energy calculations for metals and semiconductors using a plane-wave basis set. *Computational Materials Science* **1996,** 6, (1), 15-50.
50. Deák, P.; Aradi, B.; Frauenheim, T.; Janzén, E.; Gali, A., Accurate defect levels obtained from the HSE06 range-separated hybrid functional. *Physical Review B* **2010,** 81, (15), 153203.
51. Van de Walle, C. G.; Janotti, A., Advances in electronic structure methods for defects and impurities in solids. *physica status solidi (b)* **2011,** 248, (1), 19-27.
52. Adolph, B.; Furthmüller, J.; Bechstedt, F., Optical properties of semiconductors using projector-augmented waves. *Physical Review B* **2001,** 63, (12), 125108.
53. Blöchl, P. E., Projector augmented-wave method. *Physical Review B* **1994,** 50, (24), 17953-17979.
54. Kresse, G.; Joubert, D., From ultrasoft pseudopotentials to the projector augmented-wave method. *Physical Review B* **1999,** 59, (3), 1758-1775.
55. Janotti, A.; Van de Walle, C. G., LDA + U and hybrid functional calculations for defects in ZnO, SnO2, and TiO2. *physica status solidi (b)* **2011,** 248, (4), 799-804.
56. Monkhorst, H. J.; Pack, J. D., Special points for Brillouin-zone integrations. *Physical Review B* **1976,** 13, (12), 5188-5192.
57. Kumagai, Y.; Oba, F., Electrostatics-based finite-size corrections for first-principles point defect calculations. *Physical Review B* **2014,** 89, (19), 195205.
58. Petretto, G.; Bruneval, F., Comprehensive Ab Initio Study of Doping in Bulk ZnO with Group-V Elements. *Physical Review Applied* **2014,** 1, (2), 024005.
59. Qian, G.-X.; Martin, R. M.; Chadi, D. J., First-principles study of the atomic reconstructions and energies of Ga- and As-stabilized GaAs(100) surfaces. *Physical Review B* **1988,** 38, (11), 7649-7663.

60. Zhang, S. B.; Northrup, J. E., Chemical potential dependence of defect formation energies in GaAs: Application to Ga self-diffusion. *Physical Review Letters* **1991,** 67, (17), 2339-2342.
61. Walle, C. G. V. d.; Neugebauer, J., First-principles calculations for defects and impurities: Applications to III-nitrides. *Journal of Applied Physics* **2004,** 95, (8), 3851-3879.
62. Amini, M. N.; Saniz, R.; Lamoen, D.; Partoens, B., Hydrogen impurities and native defects in CdO. *Journal of Applied Physics* **2011,** 110, (6), 063521.
63. Kołodziejczak-Radzimska, A.; Markiewicz, E.; Jesionowski, T., Structural Characterisation of ZnO Particles Obtained by the Emulsion Precipitation Method. *Journal of Nanomaterials* **2012,** 2012, 1-9.
64. Landau, L. D.; Lifsic, E. M., *Electrodynamics of continuous media*. Butterworth-Heinemann: Oxford, 1984.
65. Quang, L. H.; Chua, S. J.; Ping Loh, K.; Fitzgerald, E., The effect of post-annealing treatment on photoluminescence of ZnO nanorods prepared by hydrothermal synthesis. *Journal of Crystal Growth* **2006,** 287, (1), 157-161.
66. Srikant, V.; Clarke, D. R., On the optical band gap of zinc oxide. *Journal of Applied Physics* **1998,** 83, (10), 5447.
67. Thandavan, T. M.; Gani, S. M.; San Wong, C.; Md Nor, R., Enhanced photoluminescence and Raman properties of Al-Doped ZnO nanostructures prepared using thermal chemical vapor deposition of methanol assisted with heated brass. *PLoS One* **2015,** 10, (3), e0121756.
68. McCarty, R. J.; Stebbins, J. F., Investigating lanthanide dopant distributions in Yttrium Aluminum Garnet (YAG) using solid state paramagnetic NMR. *Solid State Nuclear Magnetic Resonance* **2016,** 79, 11-22.
69. Harindranath, K.; Anusree Viswanath, K.; Vinod Chandran, C.; Bräuniger, T.; Madhu, P. K.; Ajithkumar, T. G.; Joy, P. A., Evidence for the co-existence of distorted tetrahedral and trigonal bipyramidal aluminium sites in SrAl12O19 from 27Al NMR studies. *Solid State Communications* **2010,** 150, (5–6), 262-266.
70. Stoyanova, R.; Zhecheva, E.; Kuzmanova, E.; Alcántara, R.; Lavela, P.; Tirado, J. L., Aluminium coordination in LiNi1−yAlyO2 solid solutions. *Solid State Ionics* **2000,** 128, (1–4), 1-10.
71. MacKenzie, K. J. D.; Smith, M. E., *Multinuclear Solid-state NMR of Inorganic Materials*. Elsevier Science Limited: 2002, 269-330.
72. Herzfeld, J.; Berger, A. E., Sideband intensities in NMR spectra of samples spinning at the magic angle. *The Journal of Chemical Physics* **1980,** 73, (12), 6021-6030.
73. Noriega, R.; Rivnay, J.; Goris, L.; Kälblein, D.; Klauk, H.; Kern, K.; Thompson, L. M.; Palke, A. C.; Stebbins, J. F.; Jokisaari, J. R.; Kusinski, G.; Salleo, A., Probing the electrical properties of highly-doped Al:ZnO nanowire ensembles. *Journal of Applied Physics* **2010,** 107, (7), 074312.
74. Meissner, T.; Goh, S. K.; Haase, J.; Richter, M.; Koepernik, K.; Eschrig, H., Nuclear magnetic resonance at up to 10.1 GPa pressure detects an electronic topological transition in aluminum metal. *J Phys Condens Matter* **2014,** 26, (1), 015501.
75. Rasmussen, J. A.; Henkelman, G.; Hammer, B., Pyrene: Hydrogenation, hydrogen evolution, and π-band model. *The Journal of Chemical Physics* **2011,** 134, (16), 164703.
76. Binder, J. F.; Pasquarello, A., Minimum energy path and atomistic mechanism of the elementary step in oxygen diffusion in silicon: A density-functional study. *Physical Review B* **2014,** 89, (24), 245306.
77. Norman, V., The diffusion of aluminium and gallium in zinc oxide. *Australian Journal of Chemistry* **1969,** 22, (2), 325-329.